ADVANCED OPTICAL MATERIALS

www.advopticalmat.de

Energy Yield Modeling of Bifacial All-Perovskite Two-Terminal Tandem Photovoltaics

*Fabrizio Gota, Sophie X. An, Hang Hu, Bahram Abdollahi Nejand, and Ulrich W. Paetzold**

All-perovskite two-terminal tandem photovoltaics offer high power conversion efficiencies (PCEs) that can surpass the limits of single-junction photovoltaics. In this study, energy yield (EY) simulations are performed to assess the performance of bifacial all-perovskite tandem solar cells. Under standard test conditions, in the absence of albedo, bifacial tandems demonstrate a 4.9% relative lower PCE compared to equivalent monofacial tandems due to transparency losses at the semitransparent rear side. However, under realistic irradiation conditions, albedo irradiation leads to an enhancement in EY for bifacial cells. This enhancement enables bifacial cells to produce more energy than monofacial cells, even over relatively low average reflectance (R_A) ground such as dark sandstone (R_A = 9%). The EY gain for bifacial cells rises to a maximum of 40–50% for ground modeled as a perfect reflector (R_A = 100%), accompanied by a shift in optimum top subcell bandgap to 1.56 eV. This shift is of particular interest as low-bandgap perovskite semiconductors (with lower bromide concentrations) offer enhanced stability under realistic operation conditions. Finally, this work presents a route to increase the PCE of simulated monofacial and bifacial cells, to 31.9% and 30.8%, respectively, by optimizing the optical and electrical performance of the cells.

1. Introduction

Market-dominating crystalline silicon (c-Si) single-junction (SJ) solar cells have demonstrated record power conversion efficiencies (PCE) approaching their practical limit of ≈29%.[1,2] To overcome this limit, and consequently further decrease the levelized cost of electricity (LCOE), new solutions are required. A promising approach is to employ tandem solar cells, as the theoretical PCE limit for double-junction tandem solar cells lies beyond 40%.[3] Perovskite-based tandem solar cells have attracted enormous attention in recent years, due to the remarkable optoelectronic properties[4] of metal halide perovskites, their inexpensive fabrication processes,[5,6] and tunable bandgap.[7,8] Indeed, perovskite/silicon two terminal (2T) tandem solar cells have already achieved PCEs of up to 31.25%.[9] As an alternative, all-perovskite 2T tandem solar cells, incorporating two or more perovskite layers with different bandgaps as absorber materials, are a promising new technology,[10–14] reaching record PCE of 26.4%[15] in small scale cells. This thin film technology enables the fabrication of cheap and flexible cells with extremely low energy payback time.[16] While module scale progress has not achieved the same record PCE, a recent module with a PCE of 19.1%, fabricated with a fully up-scalable layer stack, was reported by Abdollahi Nejand et al.,[17] combining a 1.26 eV bandgap bottom subcell with a 1.78 eV bandgap top subcell. This combination of bandgaps is already close to the optimum for opaque architectures estimated by Hörantner et al. of around 1.83 eV for the perovskite top subcell with a perovskite bottom subcell bandgap of 1.26 eV.[18] However, perovskite compositions with bandgaps larger than 1.68 eV (via increased bromide concentrations) are more sensitive to photoinduced phase segregation,[8] leading to faster degradation of the cells, and show increased open circuit voltage (V_{OC}) losses.[8,19,20] A bifacial architecture is a potential remedy for this issue as bifacial architecture are proven to reduce the optimum bandgap of the perovskite top subcell below the phase segregation threshold for perovskite/silicon tandem solar cells.[21,22] Furthermore, bifacial architectures greatly increase the energy yield (EY) of cells compared to the monofacial architecture.[21,22] In a bifacial architecture, the rear metal contact is replaced with a transparent conductive oxide (TCO)/encapsulation/glass layer stack, so that light can be also harvested at the rear side of the cell (see **Figure 1**). Since both high- and low-energy photons entering the cell at the rear side are absorbed in the bottom subcell, a larger current in the

F. Gota, H. Hu, B. Abdollahi Nejand, U. W. Paetzold
Institute of Microstructure Technology
Karlsruhe Institute of Technology
Hermann-von-Helmholtz-Platz 1
76344 Eggenstein-Leopoldshafen, Germany
E-mail: ulrich.paetzold@kit.edu

F. Gota, S. X. An, H. Hu, B. Abdollahi Nejand, U. W. Paetzold
Light Technology Institute
Karlsruhe Institute of Technology
Engesserstrasse 13, 76131 Karlsruhe, Germany

The ORCID identification number(s) for the author(s) of this article can be found under https://doi.org/10.1002/adom.202201691.

DOI: 10.1002/adom.202201691

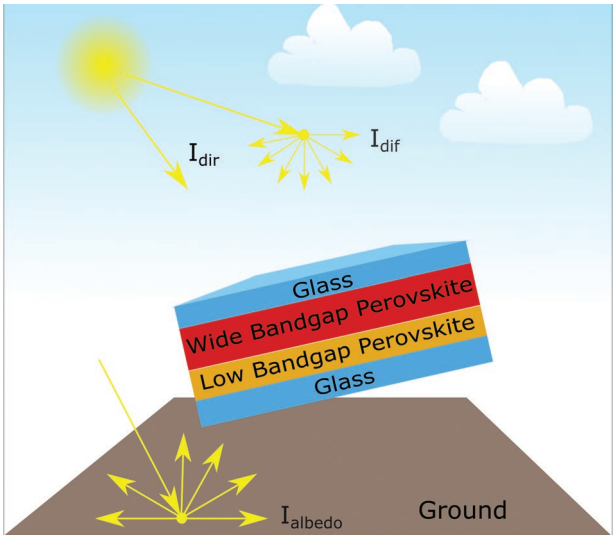

Figure 1. Schematic illustration of the working principle of bifacial all-perovskite 2T tandem solar cells under realistic irradiation conditions. Three types of irradiation can be distinguished: i) direct irradiation, emitted directly by the sun with a definite angle, ii) diffuse irradiation, which is scattered isotropically after the interaction with the atmosphere and the clouds, and iii) albedo irradiation, which is the result of scattering of direct and diffuse irradiation at the ground. The albedo irradiation is a function of the reflectance of the specific ground material. All three irradiation types play a role in front and rear illumination. However, front irradiance is mostly comprised of direct and diffuse light, while rear irradiance is dominated by albedo light.

top subcell is required to compensate for the effects of rear-side illumination.[23] Therefore, an inverse relationship is expected between optimum absorber bandgap and albedo irradiance intensity.

Assessing performances of bifacial all-perovskite 2T tandem solar cells via experimentation is a tedious and complex task. Standard test conditions (STCs) typically only include front-side illumination, with a dedicated setup required to illuminate the rear side. However, even with rear illumination, the resulting irradiation conditions will be very different from real outdoor conditions, where diffuse irradiation plays an important role and rear irradiation is the result of direct and diffuse irradiation scattering at the ground. Thus, EY simulations under realistic irradiation conditions are pivotal to develop design rules and investigate EY trends for bifacial all-perovskite 2T tandem solar cells.

In this work, in-depth EY simulations are carried out, using our in-house developed EY simulation platform EYcalc, published as an open source software.[24] First, the optical and electrical performance of the studied cells are modeled, using the high-efficiency monofacial all-perovskite 2T tandem solar cell reported by Abdollahi Nejand et al.[17] as a general reference. The bifacial cell is derived from the monofacial architecture by replacing the rear metal electrode with a transparent TCO and rear side encapsulation layer followed by a sheet glass. The perovskite top subcell bandgap and thickness of the two cells are optimized under STCs and realistic irradiation conditions with different types of ground. The EY simulations are performed for various locations with different climatic conditions and to test the dependence of bifacial cells on different albedo conditions. Finally, monofacial and bifacial cells are optically and electrically optimized to assess the potential of this technology and EY comparisons with state-of-the-art solar cell technologies are carried out. Simulations occur at cell level, neglecting the shading losses that occur for large modules under realistic operation conditions. However, we will also discuss how shading losses would quantitatively affect the results.

2. Results and Discussions

The layer stacks used in our study for both monofacial and bifacial all-perovskite 2T tandem solar cells are shown in **Figure 2**a. These layer stacks largely follow those reported by Abdollahi Nejand et al.[17] for their high-efficiency monofacial cell (for a direct comparison between experimental EQE and reflectance data with simulation results see Figure S1, Supporting Information). The bandgap of the perovskite bottom subcell is 1.26 eV. The bandgap of the top subcell is varied from 1.56 to 2.12 eV. Both monofacial and bifacial cells constitute of subcells in p-i-n architecture, with a 210 nm IO:H layer as front TCO, deposited on top of a glass substrate including a 100 nm MgF_2 anti reflection coating (ARC). A self-assembled 2PACz monolayer acts as hole transport layer (HTL) for the top subcell (the optical effects of this monolayer are deemed negligible and therefore 2PACz is not considered in the optical simulations). Following the narrow bandgap perovskite absorber, a 20 nm C_{60} layer and 20 nm SnO_2 layer serve as passivation and electron transport (ETL) layers respectively for the top subcell. The recombination junction (RJ) consists of an indium tin oxide (ITO) layer of 30 nm thickness. For the bottom subcell, a 30 nm PEDOT layer serves as HTL, followed by the wide bandgap perovskite absorber and a 5 nm PCBM and 20 nm C_{60} bilayer used as an ETL. The monofacial and bifacial layer stacks only differ in the final layers of these cells. A 100 nm thick Ag rear contact is used in the monofacial cell at the rear side after the C_{60} layer. For the bifacial cell, a 130 nm ITO layer is used as rear TCO electrode, to enable light harvesting from both directions, and the stack is completed with an EVA encapsulation layer followed by a back cover glass. A 100 nm thick MgF_2 ARC is also used to allow for an efficient light incoupling of albedo irradiation. We will refer to this combination of materials at the rear side of our cells as the rear layer configuration. It is worth noting that other encapsulation materials, such as polyolefin, have proved to perform better than EVA in damp heat and thermal cycling testing.[25] However, optical characteristics of these materials are very similar to EVA and hence would not significantly affect simulation results.

2.1. Effects of Rear Layer Configuration

To investigate the effects of different rear layer configurations on the performance of monofacial and bifacial cells, we perform optical simulations. We assume front-side illumination and that the transmitted through the perovskite absorber is striking the interface between the perovskite and remaining

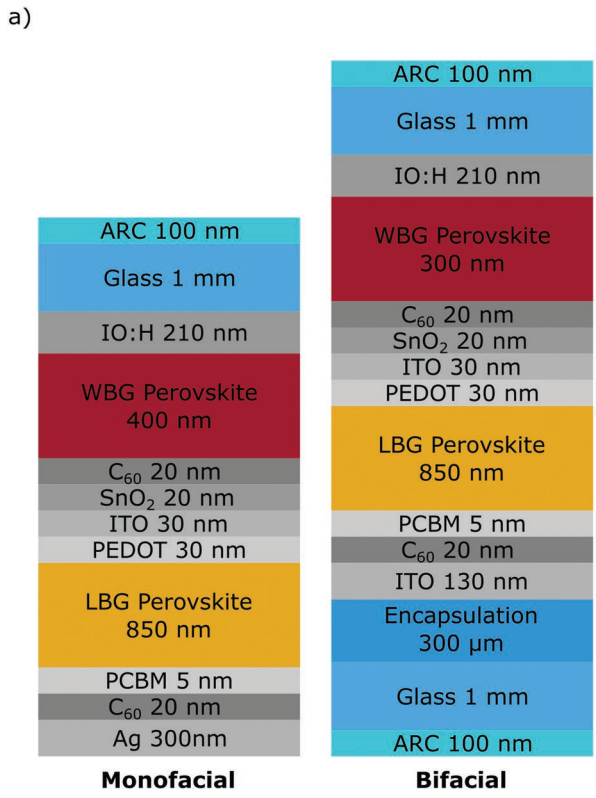

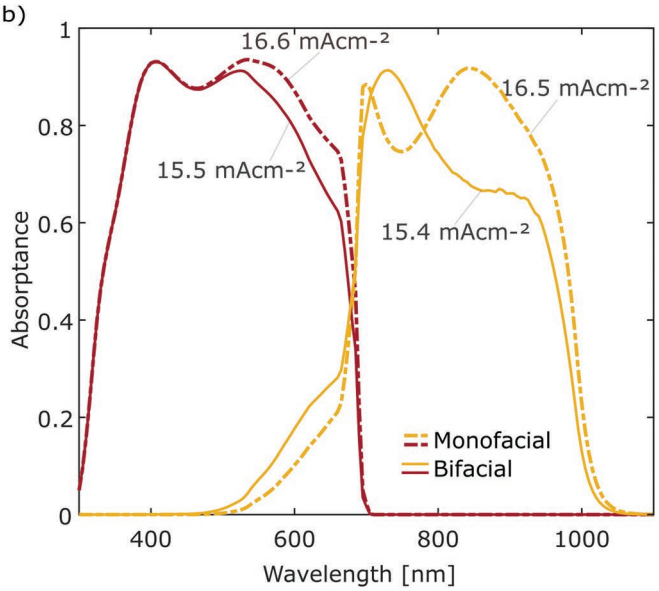

	PCE [%]	J_{SC} [mA/cm^2]	V_{OC} [V]	FF [%]
Monofacial	24.4	16.5	2.04	72
Bifacial	22.9	15.4	2.03	73

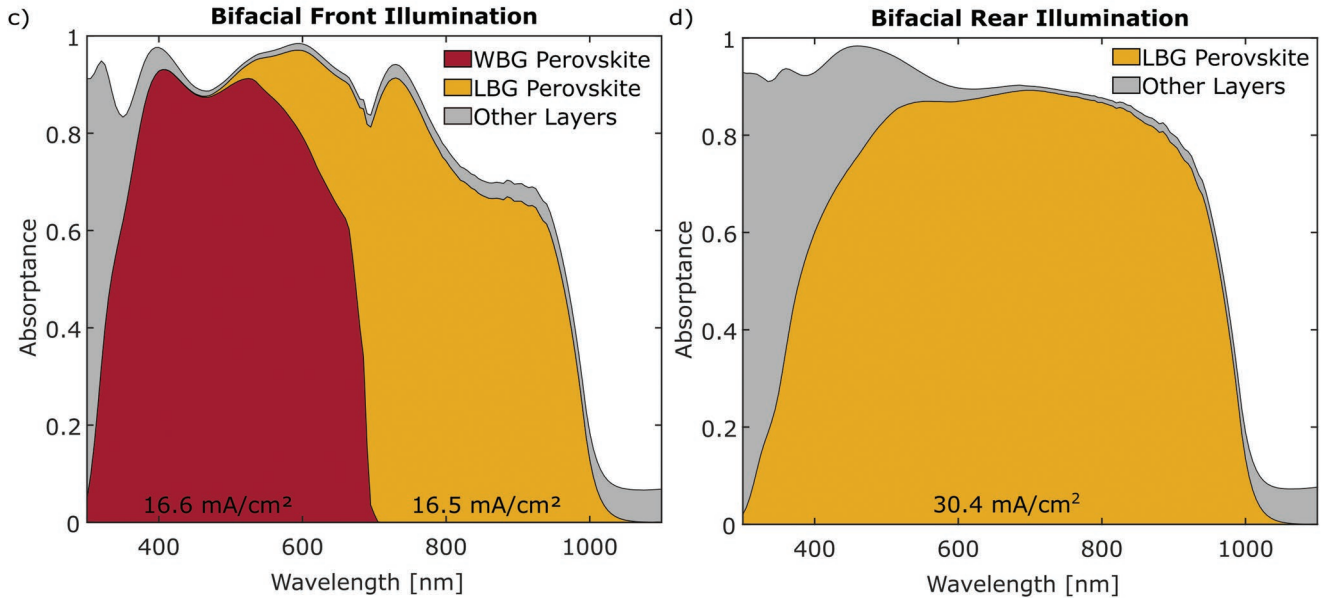

Figure 2. a) Schematic cross-section of layer stacks used for simulations in this work for monofacial and bifacial all-perovskite 2T tandem solar cells. b) Absorptance spectra for monofacial and bifacial cells. The top subcell bandgap is set to 1.78 eV, while thickness is optimized for each architecture. Absorptance spectra and parasitic losses for the bifacial cell with c) front- and d) rear-side illumination.

layers at the rear side. Then we simulate how light is reflected back into the perovskite and the transmittance through these rear layers. Due to the presence of the Ag rear electrode in the monofacial all-perovskite tandem solar cell, the average reflectance from the rear layers in the 700–1200 nm wavelength range is equal to 96%. For the bifacial architecture only 4% of the light is reflected back at normal incidence, while 94% is outcoupled from the cell at the rear side (for reflectance at the rear side for monofacial and bifacial cells see Figure S2, Supporting Information). As a consequence, under STCs, a loss in short-circuit current density of 1.1 mA cm^{-2} is expected for the bifacial cell compared to the monofacial reference. The loss in

bottom subcell photogenerated current density leads to a lower optimal top subcell thickness in the bifacial cell compared to the monofacial cell in order to achieve current matching (see Figure 2b). By inputting photogenerated current densities into the electrical module, we find that the monofacial cell achieves a ≈7% relative increase in PCE (24.4% for monofacial, 22.9% for bifacial), using a wide bandgap perovskite top subcell bandgap of 1.78 eV and modifying thicknesses to achieve current matching, due to improved light harvesting in the bottom subcell. For a detailed description of the electrical module and electrical parameters used in this work see the Experimental Section. As a result of increased current density, V_{OC} is also slightly higher for the monofacial cell (2.04 V for monofacial, 2.03 V for bifacial).

However, these simulations assume no illumination at the rear side of the bifacial cell. When illumination is introduced to the rear side, the lower optical performance of the bifacial cell with front illumination is compensated by light harvested at the rear. Assuming rear illumination with an AM1.5G spectrum, up to 30.4 mA cm^{-2} current density can be generated in the bottom subcell. However, in this theoretical situation, no light is absorbed by the top subcell, since the high energy photons typically absorbed by this subcell are already absorbed by the preceding layers, while low energy photons, with energy below the E_G of top subcell perovskite, cannot be absorbed by the top subcell. Therefore, light entering the cell from the rear side in a bifacial architecture generates extra current exclusively in the bottom subcell that can balance or even exceed front-side illumination current loss in the bottom subcell caused by the semi-transparent rear layer configuration.

2.2. Perovskite Top Subcell Bandgap and Thickness Optimization

The optimum perovskite top subcell bandgap and thickness in monofacial and bifacial cells is greatly impacted by the distribution of photogenerated current density in the two subcells and the presence of albedo light under realistic irradiation conditions. In the following, we optimize the perovskite top subcell bandgap and thickness for monofacial and bifacial cells under STCs and realistic irradiation conditions for different ground types. We optimize the perovskite top subcell bandgap in a range between 1.56 and 2.12 eV, while thickness is varied between 100 and 1000 nm.

Under STCs, the optimum top subcell bandgap for the monofacial cell is 1.82 eV, while the optimum perovskite thickness is 600 nm (see **Figure 3**a), resulting in a maximum PCE of 24.5%. As previously established, current density generation in the bottom subcell is lower for a bifacial cell without albedo compared to the monofacial scenario. To compensate for this, a wider optimum bandgap is required for the top subcell (1.86 eV), in order to increase the share of current generated in the bottom subcell. The optimum perovskite top subcell thickness is 640 nm and the maximum PCE is 23.3% (4.9% lower relative to the optimized monofacial cell).

Under realistic irradiation conditions, the optimum top subcell bandgap shifts to higher values, primarily due to the higher share of high-energy photons in diffuse irradiation. For atmospheric conditions equivalent to Phoenix, AZ (we provide more information about temperature and spectral irradiance in Phoenix in Figures S3 and S4, Supporting Information),

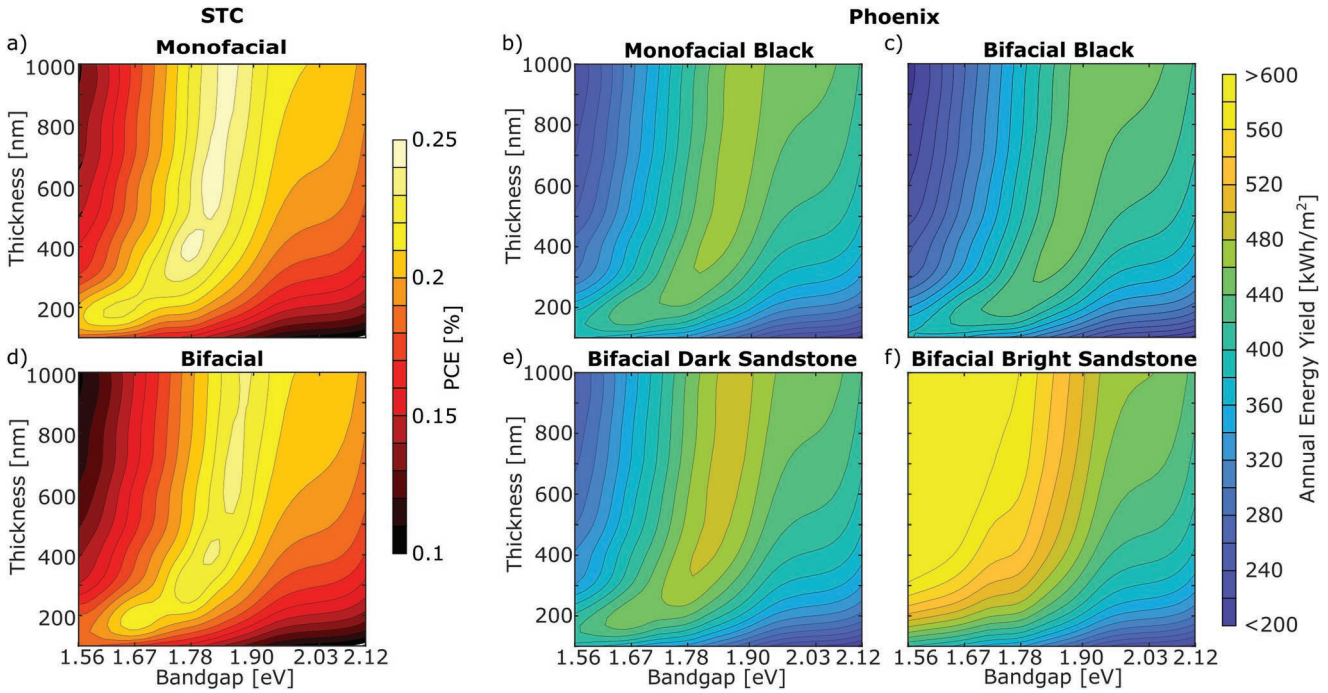

Figure 3. Power conversion efficiency (PCE) under standard test conditions (STCs) as a function of perovskite top subcell bandgap and thickness for a) monofacial and b) bifacial cells. Annual energy yield (EY) as a function of perovskite top subcell bandgap and thickness for c) monofacial and for bifacial cells with d) black background ($R_A = 0\%$), e) dark sandstone background ($R_A = 9\%$), and f) bright sandstone background ($R_A = 64\%$) in Phoenix, AZ.

the optimum perovskite top subcell bandgap is 1.89 eV for the monofacial cell and 1.92 eV for the bifacial cell, assuming a black absorber with an average albedo reflectance over the 300–1200 nm range of $R_A = 0\%$ as the ground. For the spectrally resolved reflectance of different ground types see Figure S5, Supporting Information). When albedo irradiation is considered, more light is collected by the bottom subcell. Therefore, optimum bandgap shifts to lower values and optimum perovskite top subcell thickness to higher values, in order to generate a larger share of current in the top subcell and obtain current matching (for optimum perovskite top subcell thickness as a function of perovskite top subcell bandgap for different ground types see Figure S6, Supporting Information). Even for a poorly reflective ground type as dark sandstone ($R_A = 9\%$), the optimum bandgap is 1.86 eV. For a highly reflective ground as bright sandstone ($R_A = 64\%$), optimum bandgap falls to as low as 1.61 eV (for a comparison of bifacial cells under AM1.5G spectrum and different backgrounds see Figure S7, Supporting Information). As discussed in the introduction, a narrower perovskite bandgap is desirable due to reduced degradation and increased stability, since perovskite compositions with wide-bandgaps suffer from photoinduced phase segregation.[26,27] Therefore, the bifacial architecture in all-perovskite 2T tandem solar cells, in combination with highly reflective ground, is a potential method to overcome one of the greatest issues of perovskite solar cells. Moreover, the annual EY for bifacial cells is significantly enhanced compared to monofacial cells, up to +34% with bright sandstone as ground material.

In Figure 3a,d, we notice interference patterns in the PCE for the monofacial and bifacial cells under STCs (see the gap in the contour plot between 1.80 and 1.90 eV), while these effects are less visible under realistic irradiation conditions. The all planar stack of the cells presented in this work is prone to interference effects. Under stable irradiation conditions, a variation in perovskite thickness shifts the interference patterns. These effects are smoothed out in the contour plot for cells under realistic irradiation conditions because of the continuously varying irradiation conditions.

Finally, it should be noted that all simulations presented in this work do not take into account shading losses, which would occur under realistic conditions in PV fields. Such losses comprise shading due to the module itself and due to adjacent rows of modules. The magnitude of these losses depends on parameters specific for each scenario, such as module installation height and distance between rows of modules. To discuss the impact of shading losses, we used the illumination code[28] for bifacial cells introduced by Jäger et al.[29,30] We find that shading losses at the rear side of a bifacial cell for two different realistic scenarios reduce rear albedo irradiation between 35% and 55% (see Figure S8, Supporting Information, for more details about our shading losses simulations). Since this reduction greatly depends on installation parameters, the following EY simulations disregard shading losses. The reduction due to shading losses is analogous to reducing the average albedo R_A. Therefore, to have a preliminary estimate of the impact of shading losses in our simulations, R_A should be scaled a value 35%–55% relatively lower.

In summation, our simulations show that it is necessary to further develop wide-bandgap (>1.80 eV) perovskite top subcells to explore the full potential of all-perovskite 2T tandem solar cells under STCs. However, under realistic irradiation conditions, adopting a bifacial architecture in combination with highly reflective ground, allows the use of narrower bandgap compositions while substantially increasing EY compared to monofacial cells.

2.3. Annual Energy Yield Under Different Climatic Conditions

Next, we want to identify potential EY and optimum bandgap trends under different climatic conditions. Therefore, we expand the simulations performed in the previous section by calculating the annual EY of bifacial cells in five example locations and for six different ground types (always assuming a black ground for monofacial cells) with several top subcell bandgaps in the range between 1.56 and 2.12 eV (see **Figure 4**a). The tilt angle is optimized for the monofacial cell (for an analysis of the robustness of bifacial cells to tilt angle variations see Figure S9, Supporting Information). For all five locations, the EY loss of the bifacial cell compared to the monofacial cell with a black background is ≈3–4%. For low reflective grounds such as dark sandstone ($R_A = 9\%$), there is already an EY gain for bifacial cells of ~4–5% over the monofacial cell. For higher R_A, the EY gain increases linearly, up to ≈35% for bright sandstone ($R_A = 64\%$) (see Figure 4b). Further increasing the albedo reflectance, the tandem cell is always top limited due to the large albedo current generated in the bottom subcell and therefore the EY gain of bifacial cells plateaus at ≈40–50%. The optimum perovskite top subcell bandgap decreases with increasing R_A, since more light is collected by the bottom subcell due to rear albedo irradiation. With a grass ground ($R_A = 35\%$), the optimum bandgap is decreased from 1.90 to 1.72–1.78 eV. With bright sandstone ($R_A = 64\%$), the optimum bandgap is 1.56–1.62 eV.

When considering high values of albedo reflectance ($R_A > 64\%$), the EY gain of the bifacial cell over the monofacial cell depends on the location. In particular, locations at higher latitudes show a larger EY gain in favor of bifacial cells. In Honolulu, Hawaii, the closest simulated location to the equator, the EY gain is equal to 37%, while in Anchorage, Alaska, where the latitude is highest among the locations under study, the EY gain is largest, equal to 51%. As mentioned earlier, for high values of albedo, the tandem subcell is always top limited, even when choosing the maximum thickness (1000 nm) and the narrowest bandgap (1.56 eV) investigated for the top subcell. Since at higher latitudes the cell is mounted with a larger tilt angle, more albedo light is collected by the top subcell and consequently current mismatch is reduced. Therefore, bifacial tandem cells at higher latitudes benefit more from this contribution and the EY gain over the monofacial cells with dark background is larger. However, this tilt introduces potential albedo irradiation at the front side also for monofacial cells. If we also take this into account for monofacial cells, the EY gain of bifacial cells over monofacial cells does not show a significant dependence on latitude and reaches a maximum of 35% when assuming a white background (for an analysis of front-side albedo irradiation and tilt angle optimization for monofacial all-perovskite 2T tandem cells see Figure S10, Supporting Information).

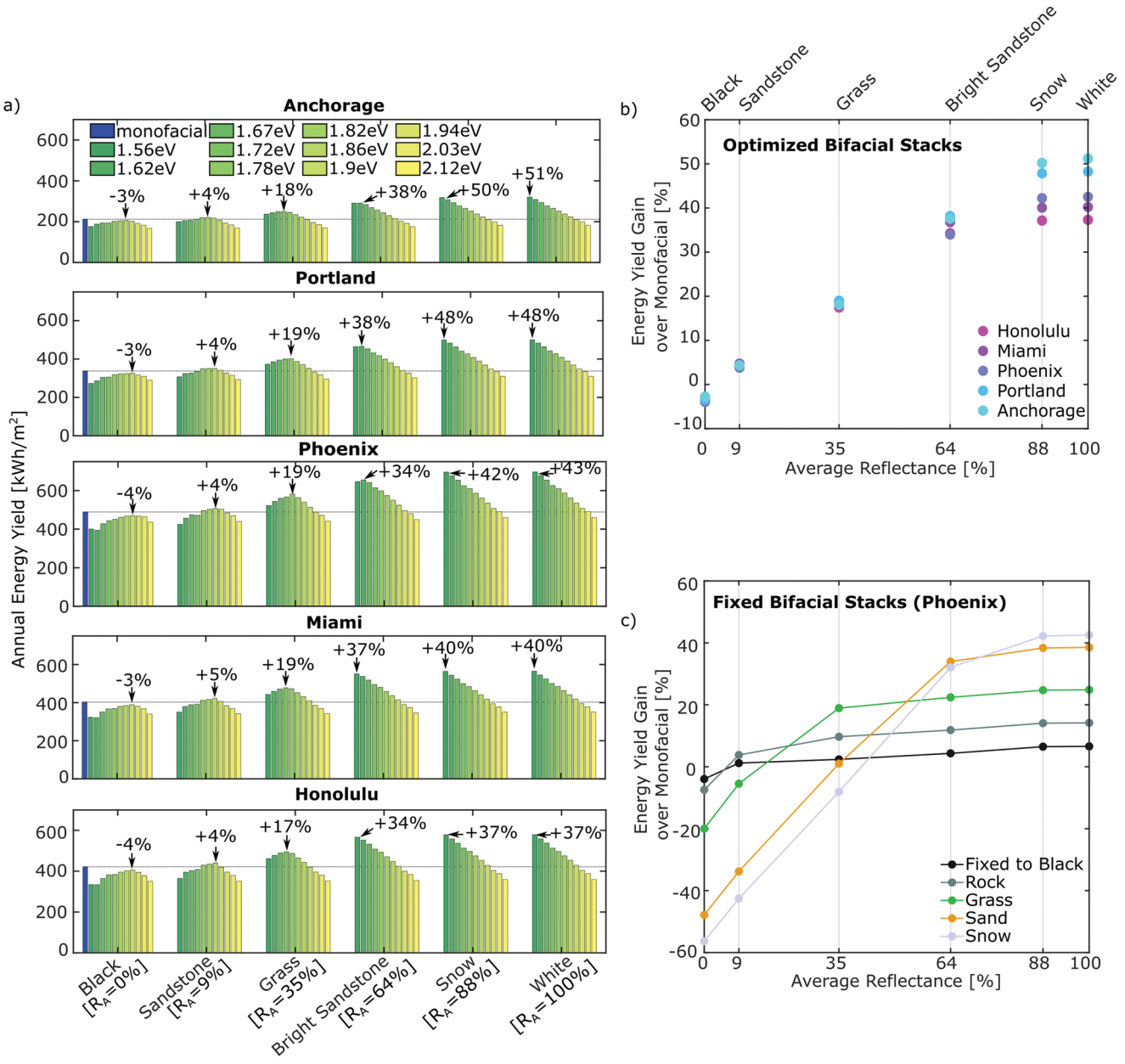

Figure 4. a) Annual EY for different ground types and perovskite top subcell bandgaps in five different locations in the USA. b) Annual EY gain of the bifacial cell over monofacial cell for different ground types and five different locations. The perovskite top subcell bandgap and thickness is optimized for each data point. c) Annual EY gain of bifacial cell over the optimized (perovskite top subcell bandgap and thickness) monofacial cell for different ground types in Phoenix. For each line, the bifacial cell is optimized for only one ground type.

Optimizing the bifacial cell architecture for each ground type can be economically challenging. As we reported in the previous section, for different ground types there is a very large variation in optimum perovskite top subcell bandgap and thickness. Optimizing the bifacial cell for different ground types would imply fabricating different versions of cells, increasing the overall cost of fabrication. To investigate the robustness in performance of bifacial cells for different albedo conditions, we optimize the cell for one ground type and then simulate the performance of the cell for all the remaining ground types (see Figure 4c). Once the cell is optimized for one albedo condition, increasing albedo does not significantly increase the annual EY. A larger albedo actually increases current generation in the bottom subcell. In this scenario, the tandem cell is top limited. Since output power largely depends on the limiting subcell, the final EY is only slightly affected, since the top subcell is not greatly affected by albedo variations. If, instead, albedo is lower than the level for which the cell was optimized, a severe EY loss is observed. In the latter scenario, the cell is now bottom limited. Since the bottom subcell current generation is greatly affected by albedo, a significant decrease in EY is observed.

2.4. Optimized Monofacial and Bifacial Cells

Up to now, results presented in this work are based on cells adapted from the high-efficiency all-perovskite 2T tandem solar cell by Abdollahi Nejand et al.[17] The former sections focus on the current state-of-the-art of the technology. However, despite showing a PCE of 24.4%, close to the highest efficiency all-perovskite 2T tandem solar cell (26.4%), performances of simulated cells predict a very large room for improvements, considering the theoretical limit (≈40%) for 2T tandem solar cells with a 1.26 eV bandgap bottom subcell.[3] Future advances are expected for passivation, charge carrier extraction and TCO layers, leading to substantial improvements in V_{OC} and FF. Moreover, materials with lower parasitic losses and improved light management can considerably increase J_{SC}. Therefore, to investigate the overall potential of all-perovskite 2T tandem solar cells under STCs and realistic irradiation conditions, electrical (V_{OC} and FF) and optical (J_{SC}) parameters of a monofacial cells with the simulated optimum top subcell bandgap (1.83 eV) are optimized under STCs with incremental steps and then simulations under outdoor irradiation conditions are performed. To achieve this, we vary dark saturation current density J_0, series resistance R_s, and shunt resistance R_{sh} for top and bottom subcells (see Table S1, Supporting Information) in electrical simulations and layer thickness (see **Figure 5**a and Table S2, Supporting Information) in optical simulations. The results for a monofacial cell are showed in Figure 5b.

Enhancing electrical performance of the cell results in a larger improvement in PCE. V_{OC} is increased from 2.06 to 2.25 V (the latter corresponding to a $q \times V_{OC,tandem}/(E_{G,bottom}+E_{G,top})$ ratio of 0.74, close to the record V_{OC}/E_G ratio of 0.76% for a high-bandgap perovskite single junction[31]) and FF from 72% to 81%. As a result, PCE increases ≈21% relative. Optimizing the layer thickness increases PCE by a mere ≈5% relative. Combining electrical and optical optimizations, PCE of the optimized monofacial cell reaches a maximum value of 31.9%, a 31% relative improvement compared to the standard cell. Performing analogous optimizations on the bifacial architecture, a PCE equal to 30.8% is achieved. Therefore, a large room for improvement is apparent for all-perovskite 2T tandem solar cells. In particular, investigating new solutions to improve electrical parameters, by developing new passivation and charge carrier extraction layers, in combination with a careful minimization of series resistance losses, are expected to boost the PCE of next generation all-perovskite 2T tandem solar cells.

The percentage gain in PCE of the optimized bifacial cell over the standard bifacial cell (see Figure 5c) matches the EY gain under realistic irradiation conditions, which is equal to ≈30% for all ground types. The EY performance of all-perovskite 2T tandem cells are also remarkable when compared to current state-of-the-art photovoltaics technologies. The EY gain for the standard all-perovskite 2T tandem cells over market dominating c-Si single junction (SJ) cells (22.2% PCE for monofacial, 21.9% PCE for bifacial cell) is ≈13% for monofacial cells, while it decreases with increasing albedo for bifacial cells. For ground types with R_A > ≈40%, bifacial c-Si SJ cells exhibit larger EY than a standard bifacial all-perovskite 2T tandem cell. However, optimized all-perovskite 2T tandem cells produce larger EY in every scenario. For monofacial cells, the EY gain of optimized all-perovskite 2T tandem cells over c-Si SJ cells is 47%, while for bifacial cells it ranges from 45% for dark ground to 8% for white ground (assuming no shading losses). When shading losses are taken into account, the total albedo irradiance decreases by ≈35–55% relative. In this scenario, even assuming an ideal white ground, the EY gain of the optimized bifacial cell over the c-Si bifacial cell is 22% to 28%. In a more realistic scenario, assuming a bright sandstone background (R_A = 64%) and shading losses, the EY gain ranges from 29% to 33%. The decrease in EY gain of bifacial all-perovskite 2T tandem cells over SJ c-Si cells for increasing albedo is due to the better albedo current management of SJ cells (no current mismatch losses). Moreover, starting from R_A = 60% (and no shading losses), tandem cells are top limited and therefore a larger albedo current does not correspond anymore to a liner increase in output power.

The large predicted EY gains of all-perovskite 2T tandem solar cells, in combination with the low fabrication costs, promise to significantly reduce the LCOE compared to current c-Si technology.

3. Conclusion

This study presents in-depth optical and EY simulations for all-perovskite 2T tandem solar cells under STCs and realistic irradiation conditions, with a focus on the bifacial architecture. First, we optimize the perovskite top subcell bandgap and thickness. Under STCs, the PCE of the bifacial cell is equal to 23.3% with an optimum bandgap of 1.86 eV. The lower efficiency compared to the monofacial cell (PCE = 24.5%, optimum bandgap 1.82 eV) is due to transparency losses for low energy photons which escape from the semitransparent rear side of the cell. When considering albedo irradiation in realistic irradiation conditions, the bifacial cell shows a 4–5% EY gain over the monofacial cell for a relative low average albedo reflectance (dark sandstone, R_A = 9%), rising to 40–50% for an ideal ground reflector (R_A = 100%). Moreover, we show that for different climatic conditions, the top subcell optimum bandgap decreases with increasing albedo irradiation, down to 1.56–1.62 eV for a bright sandstone (R_A = 64%) background. The narrower bandgap of the top subcell for the bifacial architecture circumvents a major problem with metal halide perovskites, which is photoinduced phase segregation for bandgap larger than 1.68 eV.

Finally, we simulated improved optical and electrical properties of monofacial and bifacial cells to estimate the potential of this technology. Our optimizations lead to a PCE = 31.9% for a monofacial cell and 30.8% for a bifacial cell.

Overall, bifacial all-perovskite 2T tandem solar cells represent a promising technology for high efficiency next generation photovoltaic devices, allowing superior PCE and EY performances over c-Si SJ solar cells, in addition to flexible cells and low energy payback times.

4. Experimental Section

The EYcalc EY modeling platform used for this work, which is freely accessible online,[24] has already been described in-depth by

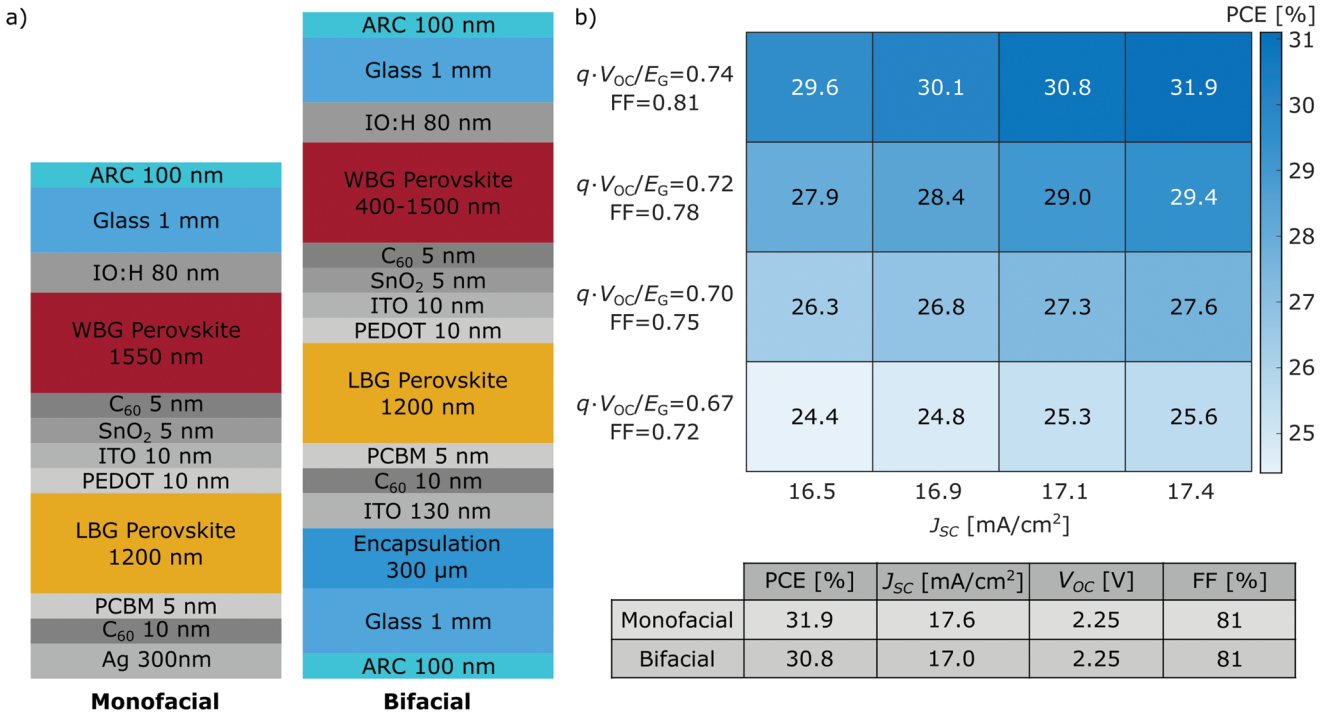

	PCE [%]	J_{SC} [mA/cm²]	V_{OC} [V]	FF [%]
Monofacial	31.9	17.6	2.25	81
Bifacial	30.8	17.0	2.25	81

Figure 5. a) Optimized monofacial and bifacial layer stacks. b) Heat map table showing the power conversion efficiency (PCE) of optimized monofacial cells for incremental improvement of J_{SC} on one axis and FF and $q \cdot V_{OC,tandem}/(E_{G,bottom} + E_{G,top})$ ratio on the other axis. The perovskite top subcell bandgap is set to 1.82 eV. c) Annual EY for monofacial and bifacial 2T tandem cells with standard and optimized stacks and for crystalline silicon (c-Si) single junction cells in Phoenix, AZ, for different ground types. The perovskite bandgap and thickness of the tandem cells is optimized for each data point.

Schmager et al.[32] Here, this work provides a concise summary of its main functions and working principles. The platform comprises four modules: (i) irradiance module, (ii) optics module, (iii) electrics module, and (iv) EY core module. The irradiance module computes direct and diffuse irradiance spectra, spectrally and angularly resolved, for each hour of a typical meteorological year. Hourly resolved typical meteorological data (TMY3)[33] from National Renewable Energy Laboratory (NREL) are fed into the simple model of atmospheric radiative transfer of sunshine (SMARTS),[34] and later into a simple cloud model, to calculate direct and diffuse irradiance over a horizontal surface. The optics module uses a combination of the transfer-matrix method for thin, optically coherent, layers and a series expansion of the Beer–Lambert law for thick, optically incoherent, layers to compute spectrally and angularly resolved reflectance, transmittance, and absorptance for each layer of the stack. Layer stacks comprising textured interfaces can also be simulated by the optics module using geometrical ray-tracing, as reported by Baker–Finch and McIntosh.[35] Next, the EY module, combining the output of the first two modules,

calculates the hourly resolved photogenerated current density (J_G) in the two absorber layers, taking into account solar cell orientation. The contributions from the direct, diffuse, and albedo irradiance are determined separately. We assume a homogeneous angular distribution of diffuse irradiance. The albedo irradiance is calculated assuming Lambertian scattering of direct and diffuse irradiance at the ground and using spectral reflection data of the ecosystem spaceborne thermal radiometer experiment on space station (ECOSTRESS) spectral library.[36,37] Then, the electrics module uses an analytical one-diode model to determine the temperature-dependent current density-voltage (*J–V*) characteristics and the maximum power point (MPP) for each set of hourly resolved J_G. Temperature effects are taken into account using temperature coefficients for the V_{OC} and J_G. The cell temperature is estimated using the Nominal Operating Cell Temperature (NOCT) model,[38] assuming NOCT = 48° and extracting the insolation on the cell and ambient air temperature from TMY3 data. The final result of the annual EY is computed by the EY core module by taking into account all the contributions from each hour of the year.

The modeling of the reference monofacial and bifacial cells was based on optical and electrical data from monofacial all-perovskite tandem solar cells from Abdollahi Nejand et al.[17] The modeling of bifacial devices under realistic irradiation conditions was already calibrated in a previous work by De Bastiani et al.,[22] where we modeled bifacial perovskite/silicon tandem solar cells based on experimental outdoor data.

The complex refractive index of the perovskite materials used for the optical simulations in this work was obtained from Hörantner et al.[18] for the bottom subcell and Ndione et al.[39] for the top subcell. The bottom subcell's refractive indices in Hörantner et al. are calculated from a $MA_{0.4}FA_{0.6}Sn_{0.6}Pb_{0.4}I_3$ perovskite layer. In Ndione et al., the top subcells' refractive indices are obtained from methylammonium lead iodide (CH_3NH_3PbI, E_G = 1.56 eV), methylammonium lead bromide (CH_3NH_3PbBr, E_G = 2.30 eV), and two intermediate compositions with a mixture of iodide and bromide. The other remaining top subcell perovskite compositions used in this work have been extracted via interpolation of the refractive indices of the original four compositions.

The electrical parameters (series resistance R_s, shunt resistance R_{sh}, and dark saturation current J_0) of the perovskite subcells are set such that the fill factor is equal to 72% and the $q \times V_{OC,tandem}/(E_{G,bottom} + E_{G,top})$ ratio is 0.68 for each top subcell bandgap. Table S3 (Supporting Information) reports the electrical parameters used for the perovskite subcells in this work, while Figure S11 (Supporting Information) shows the final value of $V_{OC,tandem}$ as a function of the perovskite top subcell bandgap.

The one-diode model used in the electrical simulations offers a good match under high illumination conditions, while under low illumination conditions a more complex double diode model offers better accuracy.[40] Moreover, we always use the minimum of the two currents generated in the subcells to compute the tandem cells' *I–V* characteristic. It has been demonstrated that in tandem cells, current mismatch induces larger FF of the tandem cell.[41]

However, it is worth noting that the key results presented here are mostly influenced by optical effects and that this model has been used for all the simulations in this work. Therefore, the conclusions drawn in this work are still valid.

Supporting Information

Supporting Information is available from the Wiley Online Library or from the author.

Acknowledgements

F.G. and S.X.A. contributed equally to this work. The authors are grateful for the support of Prof. Dr. B. S. Richards. The authors also thank T. Feeney for the support during the revision.

Open access funding enabled and organized by Projekt DEAL.

Conflict of Interest

The authors declare no conflict of interest.

Data Availability Statement

The data that support the findings of this study are available from the corresponding author upon reasonable request.;

Keywords

all-perovskite, bifacial photovoltaics, energy yield, multi-junction, optical simulations, tandem solar cells

Received: July 20, 2022
Revised: October 10, 2022
Published online:

[1] A. Richter, M. Hermle, S. W. Glunz, *IEEE J. Photovoltaics* **2013**, *3*, 1184.
[2] S. Schafer, R. Brendel, *IEEE J. Photovoltaics* **2018**, *8*, 1156.
[3] A. De Vos, *J. Phys. D: Appl. Phys.* **1980**, *13*, 839.
[4] L. N. Quan, B. P. Rand, R. H. Friend, S. G. Mhaisalkar, T. W. Lee, E. H. Sargent, *Chem. Rev.* **2019**, *119*, 7444.
[5] Z. Li, Y. Zhao, X. Wang, Y. Sun, Z. Zhao, Y. Li, H. Zhou, Q. Chen, *Joule* **2018**, *2*, 1559.
[6] S. Albrecht, B. Rech, *Nat. Energy* **2017**, *2*, 16196.
[7] A. Rajagopal, R. J. Stoddard, S. B. Jo, H. W. Hillhouse, A. K. Y. Jen, *Nano Lett.* **2018**, *18*, 3985.
[8] T. C.-J. Yang, P. Fiala, Q. Jeangros, C. Ballif, *Joule* **2018**, *2*, 1421.
[9] NREL, https://www.nrel.gov/pv/cell-efficiency.html (accessed: July 2022).
[10] T. Leijtens, R. Prasanna, K. A. Bush, G. E. Eperon, J. A. Raiford, A. Gold-Parker, E. J. Wolf, S. A. Swifter, C. C. Boyd, H. P. Wang, M. F. Toney, S. F. Bent, M. D. McGehee, *Sustainable Energy Fuels* **2018**, *2*, 2450.
[11] D. Zhao, C. Chen, C. Wang, M. M. Junda, Z. Song, C. R. Grice, Y. Yu, C. Li, B. Subedi, N. J. Podraza, X. Zhao, G. Fang, R. G. Xiong, K. Zhu, Y. Yan, *Nat. Energy* **2018**, *3*, 1093.
[12] A. F. Palmstrom, G. E. Eperon, T. Leijtens, R. Prasanna, S. N. Habisreutinger, W. Nemeth, E. A. Gaulding, S. P. Dunfield, M. Reese, S. Nanayakkara, T. Moot, J. Werner, J. Liu, B. To, S. T. Christensen, M. D. McGehee, M. F. A. M. van Hest, J. M. Luther, J. J. Berry, D. T. Moore, *Joule* **2019**, *3*, 2193.
[13] J. Tong, Z. Song, D. H. Kim, X. Chen, C. Chen, A. F. Palmstrom, P. F. Ndione, M. O. Reese, S. P. Dunfield, O. G. Reid, J. Liu, F. Zhang, S. P. Harvey, Z. Li, S. T. Christensen, G. Teeter, D. Zhao, M. M. Al-Jassim, M. F. A. M. Van Hest, M. C. Beard, S. E. Shaheen, J. J. Berry, Y. Yan, K. Zhu, *Science (80-.).* **2019**, *364*, 475.
[14] R. Lin, K. Xiao, Z. Qin, Q. Han, C. Zhang, M. Wei, M. I. Saidaminov, Y. Gao, J. Xu, M. Xiao, A. Li, J. Zhu, E. H. Sargent, H. Tan, *Nat. Energy* **2019**, *4*, 864.
[15] R. Lin, J. Xu, M. Wei, Y. Wang, Z. Qin, Z. Liu, J. Wu, K. Xiao, B. Chen, S. M. Park, G. Chen, H. R. Atapattu, K. R. Graham, J. Xu, J. Zhu, L. Li, C. Zhang, E. H. Sargent, H. Tan, *Nature* **2022**, *603*, 73.
[16] X. Tian, S. D. Stranks, F. You, *Sci. Adv.* **2020**, *6*, eabb0055.
[17] B. Abdollahi Nejand, D. B. Ritzer, H. Hu, F. Schackmar, S. Moghadamzadeh, T. Feeney, R. Singh, F. Laufer, R. Schmager, R. Azmi, M. Kaiser, T. Abzieher, S. Gharibzadeh, E. Ahlswede, U. Lemmer, B. S. Richards, U. W. Paetzold, *Nat. Energy* **2022**, *7*, 620.

[18] M. T. Hörantner, T. Leijtens, M. E. Ziffer, G. E. Eperon, M. G. Christoforo, M. D. McGehee, H. J. Snaith, *ACS Energy Lett.* **2017**, *2*, 2506.
[19] A. Zohar, M. Kulbak, I. Levine, G. Hodes, A. Kahn, D. Cahen, *ACS Energy Lett.* **2019**, *4*, 1.
[20] O. Almora, D. Baran, G. C. Bazan, C. Berger, C. I. Cabrera, K. R. Catchpole, S. Erten-Ela, F. Guo, J. Hauch, A. W. Y. Ho-Baillie, T. J. Jacobsson, R. A. J. Janssen, T. Kirchartz, N. Kopidakis, Y. Li, M. A. Loi, R. R. Lunt, X. Mathew, M. D. McGehee, J. Min, D. B. Mitzi, M. K. Nazeeruddin, J. Nelson, A. F. Nogueira, U. W. Paetzold, N. G. Park, B. P. Rand, U. Rau, H. J. Snaith, E. Unger, et al., *Adv. Energy Mater.* **2021**, *11*, 2102526.
[21] J. Lehr, M. Langenhorst, R. Schmager, F. Gota, S. Kirner, U. Lemmer, B. S. Richards, C. Case, U. W. Paetzold, *Sol. Energy Mater. Sol. Cells* **2020**, *208*, 110367.
[22] M. De Bastiani, A. J. Mirabelli, Y. Hou, F. Gota, E. Aydin, T. G. Allen, J. Troughton, A. S. Subbiah, F. H. Isikgor, J. Liu, L. Xu, B. Chen, E. Van Kerschaver, D. Baran, B. Fraboni, M. F. Salvador, U. W. Paetzold, E. H. Sargent, S. De Wolf, *Nat. Energy* **2021**, *6*, 167.
[23] J. Chantana, Y. Kawano, T. Nishimura, A. Mavlonov, T. Minemoto, *Sol. Energy* **2021**, *220*, 163.
[24] R. Schmager, U. W. Paetzold, M. Langenhorst, F. Gota, J. Lehr, https://doi.org/10.5281/ZENODO.4696257 (accessed: May 2021).
[25] R. Cheacharoen, C. C. Boyd, G. F. Burkhard, T. Leijtens, J. A. Raiford, K. A. Bush, S. F. Bent, M. D. McGehee, *Sustainable Energy Fuels* **2018**, *2*, 2398.
[26] K. A. Bush, K. Frohna, R. Prasanna, R. E. Beal, T. Leijtens, S. A. Swifter, M. D. McGehee, *ACS Energy Lett.* **2018**, *3*, 428.
[27] X. Tang, M. Van Den Berg, E. Gu, A. Horneber, G. J. Matt, A. Osvet, A. J. Meixner, D. Zhang, C. J. Brabec, *Nano Lett.* **2018**, *18*, 2172.
[28] P. Tillmann, https://doi.org/10.5281/ZENODO.3543570 (accessed: November 2019).
[29] K. Jäger, P. Tillmann, C. Becker, *Opt. Express* **2020**, *28*, 4751.
[30] K. Jäger, P. Tillmann, E. A. Katz, C. Becker, *Sol. RRL* **2021**, *5*, 2000628.
[31] S. Gharibzadeh, B. Abdollahi Nejand, M. Jakoby, T. Abzieher, D. Hauschild, S. Moghadamzadeh, J. A. Schwenzer, P. Brenner, R. Schmager, A. A. Haghighirad, L. Weinhardt, U. Lemmer, B. S. Richards, I. A. Howard, U. W. Paetzold, *Adv. Energy Mater.* **2019**, *9*, 1803699.
[32] R. Schmager, M. Langenhorst, J. Lehr, U. Lemmer, B. S. Richards, U. W. Paetzold, *Opt. Express* **2019**, *27*, A507.
[33] S. Wilcox, W. Marion, *Users Manual for TMY3 Data Sets*, National Renewable Energy Laboratory, Golden, CO **2008**.
[34] C. A. Gueymard, *Sol. Energy* **2001**, *71*, 325.
[35] S. C. Baker-Finch, K. R. McIntosh, *Prog. Photovoltaics* **2011**, *19*, 406.
[36] A. M. Baldridge, S. J. Hook, C. I. Grove, G. Rivera, *Remote Sens. Environ.* **2009**, *113*, 711.
[37] A. Sucich, B. Miller, T. Snyder, R. Bittencourt, P. Srinivasan, P. M. Lubin, G. B. Hughes, E. Cirilo, J. Madajian, Y. Wang, in *CubeSats and NanoSats for Remote Sensing II, Proc. SPIE Vol. 10769* (Eds: C. D. Norton, T. S. Pagano), SPIE, Bellingham, WA **2018**, p. 24.
[38] M. C. Alonso García, J. L. Balenzategui, *Renewable Energy* **2004**, *29*, 1997.
[39] P. F. Ndione, Z. Li, K. Zhu, *J. Mater. Chem. C* **2016**, *4*, 7775.
[40] O. Breitenstein, S. Rißland, *Sol. Energy Mater. Sol. Cells* **2013**, *110*, 77.
[41] E. Köhnen, M. Jošt, A. B. Morales-Vilches, P. Tockhorn, A. Al-Ashouri, B. Macco, L. Kegelmann, L. Korte, B. Rech, R. Schlatmann, B. Stannowski, S. Albrecht, *Sustainable Energy Fuels* **2019**, *3*, 1995.